PERSPECTIVE

Check for updates

Near-infrared fluorescent molecular probes for imaging and diagnosis of nephro-urological diseases

All publication charges for this article have been paid for by the Royal Society of Chemistry

Jiaguo Huang and Kanyi Pu [ID] *

Near-infrared (NIR) fluorescence imaging has improved imaging depth relative to conventional fluorescence imaging in the visible region, demonstrating great potential in both fundamental biomedical research and clinical practice. To improve the detection specificity, NIR fluorescence imaging probes have been under extensive development. This review summarizes the particular application of optical imaging probes with the NIR-I window (700–900 nm) or the NIR-II window (1000–1700 nm) emission for diagnosis of nephron-urological diseases. These molecular probes have enabled contrast-enhanced imaging of anatomical structures and physiological function as well as molecular imaging and early diagnosis of acute kidney injury, iatrogenic ureteral injury and bladder cancer. The design strategies of molecular probes are specifically elaborated along with representative imaging applications. The potential challenges and perspectives in this field are also discussed.

1. Introduction

Molecular imaging enables real-time and non-invasive visualization and quantification of biological processes at the cellular or molecular level in living organisms.[1] Unlike conventional imaging modalities such as X-ray computed tomography imaging, radionuclide imaging, magnetic resonance imaging and ultrasound imaging, optical imaging as a nonionizing radiation method offers unique opportunities to study multiple dynamic biological events with high spatiotemporal resolution and high sensitivity.[2] A conventional optical imaging method relies on fluorescence detection in the visible spectrum (400–700 nm).[3] However, due to severe light scattering and reabsorption, the conventional imaging method suffers from significant light attenuation and tissue autofluorescence, resulting in shallow penetration depth and low imaging sensitivity.[4,5] In contrast, fluorescence detection in the first near-infrared window (NIR-I, 700–900 nm) and the second near-infrared window (NIR-II, 1000–1700 nm) can afford deeper penetration depth with improved signal-to-background ratios (SBRs) because of reduced photon scattering and minimal tissue autofluorescence.[6,7]

Molecular probes are needed to correlate signal with biological events or molecular status in living systems.[8,9] Optical probes such as small molecular fluorophores,[10–14] fluorescent proteins,[15] inorganic nanoparticles,[16–18] semiconducting polymer nanoparticle,[19–24] single-walled carbon nanotubes,[25] etc. have been widely used and significantly improved the

performance of imaging. Such optical probes can be classified into 'always on' probes and activatable probes. 'always on' probes often serve as signal enhancing contrast agents through accumulation and retention, thus are preferential for imaging of anatomical structures and physiological function. In contrast, activatable probes switch their signals from 'off' to 'on' state only in the presence of the biomarker or molecular event of interest (Fig. 1b).[26,27] Compared with 'always on' mode, activatable probes not only give rise to higher SBRs, but also permit real-time imaging and quantification of biomarkers in living systems, which render them suitable for early diagnosis.[28,29]

The urinary system is one of the most important waste removal and regulatory systems, which consists of the kidneys, ureters, bladder and urethra (Fig. 1a).[30] The kidneys receive up to 25% cardiac output and make urine by filtering wastes and extra water from blood. Urine flows through the ureters and fills into the bladder, followed by clear out of body through the urethra.[31] Due to the local high concentration of xenobiotics, drugs and metabolic wasters, the urinary system is vulnerable to toxic exposure and easy to be infected and injured, leading to the high incidence of nephro-urological diseases such as acute kidney injury (AKI),[32] kidney stones,[33] urinary tract obstruction and infections,[34] bladder prolapse and cancer,[35,36] etc. Moreover, ureters are located very close to many important organs, such as the colon, rectum, cervix and ovaries. The special anatomical location and thin walled structure of ureters render them prone to injury during gynecologic and general surgery.[37] Thus, development of optical imaging probes is essential for highly specific anatomical and molecular imaging of the urinary system. To data, a great number of NIR fluorescence (NIRF) probes have been used for detection of various cancer,[38–43]

School of Chemical and Biomedical Engineering, Nanyang Technological University, 70 Nanyang Drive, Singapore 637457, Singapore. E-mail: kypu@ntu.edu.sg

Fig. 1 (a) Schematic illustration of the urinary system. (b) Sensing mechanisms of activatable probes and 'always on' probes. (c–e) Schematic illustration of the applications of 'always on' probes and activatable probes for imaging of kidney, ureter and bladder in different diseases models.

sentinel lymph nodes,[44] neurological diseases,[45–47] cardiovascular diseases,[48] hepatopathy.[49,50] In contrast, only a few probes have been reported for imaging diseases in the urinary system such as drug-induced AKI, iatrogenic and traumatic ureteral injury and bladder cancer (Fig. 1c–e).

Herein, we review the advances of NIRF molecular probes for imaging and diagnosis of nephro-urological diseases. In the following sections, the molecular design strategies and imaging applications of probes are elaborated along with representative examples. Lastly, the current challenges and perspectives in this field are discussed.

2. Kidney diseases

Kidney is the primary site for metabolism and excretion of metabolic products and therapeutic drugs, thus it is vulnerable to injury.[51] As such, real-time monitoring of kidney dysfunction is essential in clinical practice. To date, 'always on' probes such as CdSe/ZnS core–shell quantum dots,[52] silica Cornell dots[53] and zwitterionic fluorophore ZW800,[54] gold nanoclusters (AuNPs),[55] etc. have been reported to go through renal clearance, and some of them have been used to imaging of kidney dysfunction. Moreover, several activatable probes have been developed for imaging and early diagnosis of AKI through
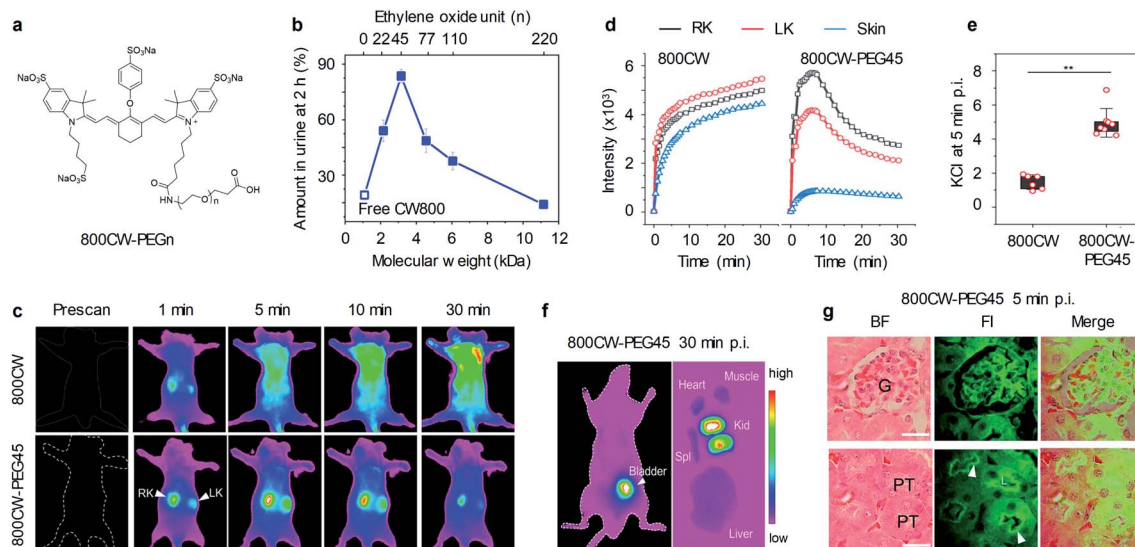

Fig. 2 (a) Chemical structures of **800CW-PEGn**; n represents the number of repeat ethylene oxide units. (b) Renal clearance efficiencies (RCE) of **800CW-PEGn** at 2 h post-intravenous injection (p.i.) as functions of molecular weight and the number of repeat ethylene oxide units. (c) Representative NIRF images of mice before and after intravenous injection of **800CW** and 800CW-PEG45. NIRF images acquired at 790 nm following excitation at 720 nm. (d) The dynamic NIRF intensities of kidneys and skin as a function of time post-injection of **800CW** and 800CW-PEG45. (e) The kidney contrast index (KCI) at 5 min post-injection of **800CW** and 800CW-PEG45. **p < 0.005. (f) Representative NIRF images of the ventral side of mice and ex vivo images of excised kidneys (kid), liver, spleen (spl), heart, and muscle at 30 min post-injection of 800CW-PEG45. (g) Representative haematoxylin and eosin (H&E) staining and fluorescence images of glomerulus and tubules from kidney slices at 5 min post-injection of 800CWPEG45. Glomerulus (G); proximal tubule (PT). Scale bar: 20 μm. Reproduced with permission from ref. 63. Copyright 2019 American Chemical Society.

detection of AKI-associated biomarkers (such as reactive oxygen species (ROS), enzymes *e.g.* *N*-acetyl-β-ᴅ-glucosaminidase (NAG), γ-glutamyl transferase (GGT) and caspase-3).[56–62]

2.1. Kidney dysfunction

Zheng and co-workers developed a series of **800CW-PEG*n*** and investigated the sub-10 kDa PEGylation effect on the renal clearance efficiency in living mice.[63] Five PEG molecules with different ethylene oxide units (22, 45, 77, 110 and 220) were used to conjugate with IRDye800CW (**800CW**) to afford corresponding **800CW-PEG*n*** (Fig. 2a), which exhibited identical optical spectra of free **800CW**. The renal clearance efficiencies of **800CW** and **800CW-PEG*n*** were determined by fluorescent quantification of urine after intravenous injection. 19.2%, 54.1%, 83.7%, 48.7%, 37.7%, and 14.1% injection dose (ID) of **800CW**, 800CW-PEG22, 800CW-PEG45, 800CW-PEG77, 800CW-PEG110, and 800CW-PEG220 were cleared into urine at 2 h post-injection, respectively (Fig. 2b). It was found that there was an inverse PEG-length dependency in renal clearance of **800CW-PEG*n***, distinct from the prevailing understanding that larger PEGylation more easily reduces the glomerular filtration of parent fluorophore than smaller ones. PEG45 is an optimized PEG moiety to generate the most efficient renal clearance for **800CW**. However, a PEG ligand either smaller or larger than PEG45 can cause a lower renal clearance.

To further study the *in vivo* clearance of **800CW** and **800CW-PEG*n***, whole body NIRF imaging was conducted on mice at different time points post-injection of **800CW** or 800CW-PEG45. At 1 min post-injection of **800CW**, the signals of **800CW** from the kidneys were observed but quickly overshadowed by the signals from the skin, leading to indiscernibility of the kidneys at later time points (Fig. 2c and d). In contrast, the kidneys were clearly delineated for a duration of 30 min after administration of 800CW-PEG45. In addition, the signals of 800CW-PEG45 from the kidneys were much higher than that of skin, resulting in the kidney contrast index (KCI) being 3.4-fold higher than that of **800CW** (Fig. 2e). Such rapid renal clearance of 800CW-PEG45 resulted in strong NIRF signals in the kidneys and bladder at 30 min and negligible signals in other organs including the liver, spleen, and heart (Fig. 2f). Noted that NIRF signals of 800CW-PEG45 in the glomerulus and proximal tubular lumen were clearly captured by confocal imaging at 5 min post-injection (Fig. 2g), indicating that 800CW-PEG45 was filtered through the glomerulus into the tubular lumen. Thus, 800CW-PEG45 with fast renal clearance and reduced nonspecific interactions enabled to imaging the kidneys with high SBR.

In addition to small molecular fluorophores, Zheng and co-workers have developed renal-clearable AuNPs by using glutathione (GSH) for surface modification (Fig. 3a).[64] The obtained GS-AuNPs had a core size of 2.5 nm and an average hydrodynamic diameter (HD) of 3.3 nm and exhibited intrinsic NIR emission at 830 nm as well as behaviours similarly to **800CW** in terms of physiological stability and renal clearance. By virtue of high resistance to serum protein adsorption, its renal clearance efficiency reached up to 50% ID at 48 h post-injection, no severe accumulation in the reticuloendothelial system organs was observed.

Fig. 3 (a) Schematic illustration of GS-AuNPs. (b) A UUO mouse model was generated by complete ligation of one ureter for 7–9 days while the other one was kept intact. In the sham control group, the left ureter was exposed but not ligated. (c) Representative NIRF images of mice at different time points post-injection of GS-AuNPs. NIRF images acquired at 830 nm following excitation at 710 nm. (d and e) The dynamic NIRF intensities of the kidneys and skin as a function of time post-injection of GS-AuNPs in the sham control group and the UUO mice group. Reproduced with permission from ref. 64. Copyright 2016 John Wiley and Sons.

To validate the ability of GS-AuNPs for imaging of kidney dysfunction, a unilateral ureteral obstruction (UUO) mouse model was generated by complete ligation of one ureter for 7–9 days while the other one was kept intact (Fig. 3b). Such UUO mice were asymptomatic at an early stage but could cause kidney dysfunction if not treated timely. While in the sham control group, both of ureters were not ligated. At 1 min post-injection of GS-AuNPs, the obstructed left kidney exhibited dramatically reduced NIRF signal relative to the contralateral right kidney in UUO mice. However, NIRF signals of both the kidneys in the sham control group were identical after injection of GS-AuNPs (Fig. 3c and d). Such a reduced NIRF signal in the left kidney of UUO mice was attributed to dramatically reduced blood perfusion after obstruction, leading to an unequal accumulation of GS-AuNPs in two kidneys (Fig. 3e).

Noted that no significant differences in blood urea nitrogen (BUN) and serum creatinine (sCr) were observed between the UUO mice and the sham control group at 7–9 days of post-operation, which was in agreement with previous studies that BUN and sCr were insensitive indicators for monitoring kidney

function in a UUO mouse model.[65] While GS-AuNPs can real-time detect kidney dysfunction in this model.

Although 800CW-PEG45 and GS-AuNPs have been used for real-time imaging of kidneys, they can only emit light in the NIR-I window, which has limited penetration depth and moderate tissue autofluorescence. To increase the optical imaging depth, our group developed a highly renal-clearable molecular semiconductor (**CDIR2**) for NIR-II fluorescent imaging of kidney dysfunction (Fig. 4a).[66] **CDIR2** was comprised of a NIR-II fluorophore and (2-hydroxypropyl)-β-cyclodextrin (HPβCD). HPβCD has been demonstrated as an excellent renal-clearance scaffold by Huang and co-workers.[67,68] **CDIR2** had an absorption peak at 770 nm and an emission peak at 1050 nm with a fluorescence quantum yield (Φ) of 2.2% in PBS (Fig. 4c). *In vitro* tissue penetration studies proved that **CDIR2** had not only deeper tissue penetration but also higher sensitivity than NIR-I fluorophore indocyanine green (ICG), which was ascribed to reduced light scattering and tissue absorption in the NIR-II window. **CDIR2** had a high renal clearance efficiency of $87 \pm 2.3\%$ ID at 24 h post-injection (Fig. 4d) and was much higher than that of NIR-II fluorophore without HPβCD conjugation ($3.8 \pm 0.7\%$ ID).

In general, renal clearance involves three pathways including glomerular filtration, tubular secretion and tubular reabsorption (Fig. 4b).[66] Glomerular filtration is the first step in renal clearance, followed by tubular secretion (from peritubular capillaries to tubular lumen) and reabsorption (from tubular lumen to the circulatory system). Both of tubular reabsorption and secretion are mediated by the organic anion and cation transporters (OAT and OCT) in renal tubular cells.[69] Whole body NIR-II fluorescence imaging was conducted in three groups of living mice treated with saline, inhibitor probenecid or cimetidine. The results demonstrated **CDIR2** was exclusively cleared *via* glomerular filtration without secretion and reabsorption in renal tubules.

To investigate the ability of **CDIR2** for real-time imaging of kidney dysfunction, NIR-II fluorescence imaging was conducted in a mouse model of cisplatin-induced nephrotoxicity. The profile for the signals in the kidneys and bladder as a function of post-injection time remained similar to saline-treated group when cisplatin post-treatment time was no more than 48 h (Fig. 4e and f). However, at 72 h post-treatment of cisplatin, the signal in the kidneys decreased and the signal in the bladder increased much slower, suggesting **CDIR2** retention in the kidneys (Fig. 4f and g). Furthermore, the visualization of bladder was delayed after 20 min injection of **CDIR2** in mice. Noted that significant increase in BUN and sCr were observed at 72 h post-treatment of cisplatin. Therefore, the kidney

Fig. 4 (a) Chemical structures of **CDIR2** (R$_2$ = H or CH$_2$CHOHCH$_3$). (b) Schematic illustration of a nephron structure and renal clearance pathways including glomerular filtration, tubular secretion and tubular reabsorption. (c) Absorption and fluorescence spectra of **CDIR2** in PBS (10 mM, pH 7.4). (d) RCE as a function of time post-injection of **CDIR2** in living mice. The three lines represent the measurements in three independent mice. (e) Representative NIR-II fluorescence images of living mice after intravenously injection of **CDIR2** (1 mmol per kg body weight) at different post-treatment time points (24, 48 or 72 h). The control groups were treated with saline. (f and g) The dynamic NIR-II fluorescence intensities of the kidneys and bladder as a function of time post-injection of **CDIR2** in living mice treated with saline or cisplatin at different post-treatment time points. Reproduced with permission from ref. 66. Copyright 2019 John Wiley and Sons.
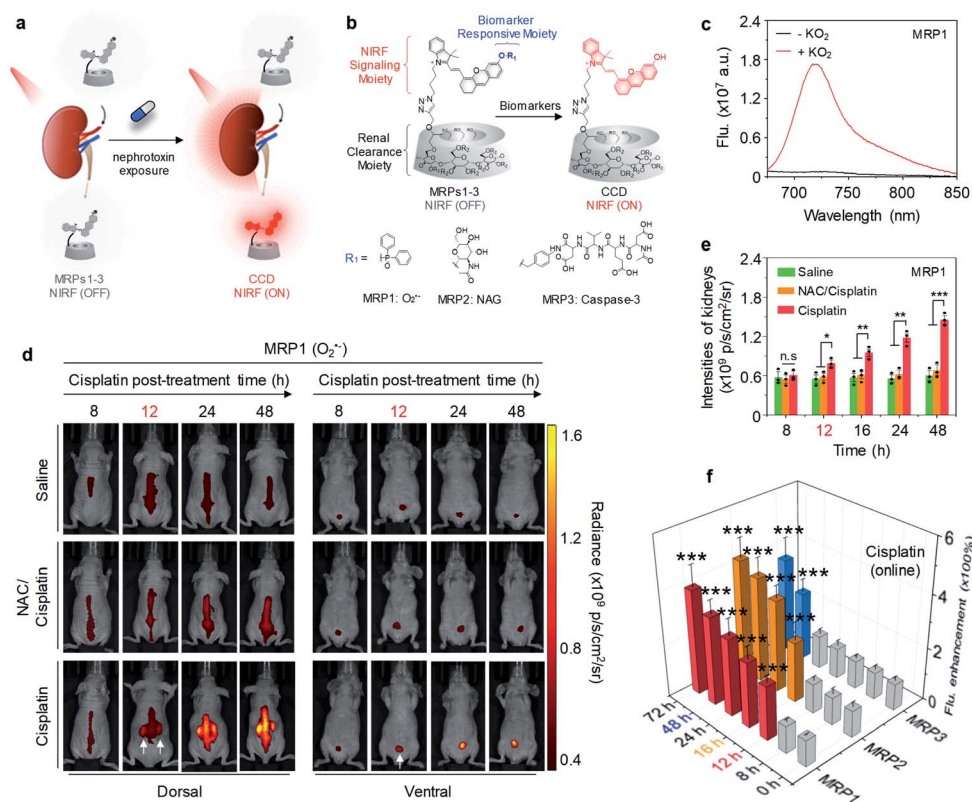
Fig. 5 (a) Schematic illustration of NIRF imaging of drug-induced AKI using **MRPs1–3**. (b) Chemical structures and molecular mechanisms of **MRPs1–3** and their activated forms in response to $O_2^{\bullet-}$, NAG and caspase-3, respectively, (R = H or $CH_2CHOHCH_3$). (c) Fluorescence spectra of **MRP1** (30 μM) in the absence or presence of KO_2 (60 μM) in PBS buffer (10 mM, pH 7.4). (d) Representative NIR fluorescence images of living mice with injection of **MRP1** after treatment of cisplatin (20 mg per kg body weight) for 8, 12, 24 or 48 h. The control groups were treated with PBS or a nephroprotective antioxidant NAC. NIRF images acquired at 720 nm upon excitation at 675 nm. (e) NIRF intensities of kidneys in living mice after 30 min injection of **MRP1** at the different post-treatment time points (8, 12, 16, 24 or 48 h). (f) Fluorescence enhancement of excreted **MRPs1–3** in the urine from cisplatin-treated living mice after injection at different time points post-treatment of cisplatin. n.s: not significant, *$p < 0.05$, **$p < 0.01$, ***$p < 0.001$. Reproduced with permission from ref. 56. Copyright 2019 Springer Nature.

dysfunction detection ability of **CDIR2** was consistent with clinical diagnostic assays.

2.2. AKI

Although above probes can undergo renal clearance and are feasible for kidney imaging, they relied on the passive retention in blocked kidneys to obtain a signal readout, and thus are unable to delineate the early molecular events of kidney injury. In contrast to those 'always on' probes, activatable probes can specifically monitor the biomarkers with an active sensing mechanism, permitting detection of kidney injury at the early stage.

Our group reported molecular renal probes (MRPs) for real-time NIRF imaging and early diagnosis of drug-induced AKI (Fig. 5a).[56] MRPs were constructed on a hemi-cyanine precursor wherein the aromatic hydroxyl group was caged with biomarkers reactive moieties, which included diphenylphosphinyl, N-acetyl-β-D-glucosaminide and a tetrapeptide sequence (Asp–Glu–Val–Asp) that respond to superoxide anion ($O_2^{\bullet-}$), NAG and caspase-3 for **MRP1**, **MRP2** and **MRP3**, respectively. The azide group on the alkyl chain was conjugated with HPβCD (Fig. 5b). Because the three MRPs (**MRPs1–3**) had

similar optical profiles, **MRP1** was selected as an example. **MRP1** was initially non-fluorescent because the electron donating ability of the aromatic hydroxyl group was diminished. Upon addition of KO_2, the fluorescence of **MRP1** at 720 nm increased by 21-fold and the limit of detection (LOD) was determined to be 11 nM (Fig. 5c).

After confirming its high renal clearance efficiency (92% ID at 24 h post-injection), the ability of **MRP1** for real-time imaging of $O_2^{\bullet-}$ was evaluated in a mouse model of cisplatin-induced AKI. At 8 h post-treatment with cisplatin, the signals from **MRP1** in the kidneys were as low as that of the control mice (Fig. 5d). However, at 12 h post-treatment with cisplatin, the kidneys were clearly delineated with NIRF imaging, showing a 1.45-fold signal increase relative to the control mice. The NIRF signals of **MRP1** in the kidneys further increased at later post-treatment time points (Fig. 5e), implying the gradual upregulation of $O_2^{\bullet-}$. Similar phenomena were observed for **MRP2** and **MRP3**, but their earliest detection time points were 16 and 48 h post-treatment with cisplatin, respectively, indicating cisplatin first induced oxidative stress followed by lysosomal damage and apoptosis. Besides, direct fluorescence measurement of excreted **MRPs1–3** in the urine from cisplatin-treated mice after

intravenous injection was carried out. The results were coincided with the real-time NIRF imaging data *in vivo* (Fig. 5f), because the excreted **MRPs1–3** were activated in the kidneys followed by excretion into urine. Such an active sensing mechanism of **MRPs1–3** enabled detect drug-induced AKI prior to kidney function decline and histological changes, outperforming the typical clinical assays in terms of detecting AKI at least 36 h earlier.

Later, we further synthesized a renal clearable chemo-fluoroluminescent probe for crosstalk-free chemiluminescence and NIRF imaging of contrast-induced AKI (CIAKI). Such an activatable duplex reporter can detect CIAKI prior to renal function decline at least 8 h.[57]

Very recently, our group further reported a fluorophotoacoustic polymeric renal reporter (**FPRR**) for NIRF and photoacoustic (PA) dual imaging of cisplatin induced-AKI (Fig. 6a).[58] GGT, a brush border enzyme highly expressed in proximal tubular epithelial cells, is released during AKI. Thus, GGT was chosen as the targeted biomarker for the design of **FPRR**. Instead of HPβCD, dextran has been used as a renal clearance moiety. In the presence of GGT, γ-glutamate of **FPRR** can be cleaved, followed by elimination and spontaneous release of **Dex-CD**, leading to a 33-fold increase in NIRF signals at 710 nm and a 6.5-fold enhancement in PA signal at 700 nm (Fig. 6b and c). The renal clearance efficiency of **FPRR** was determined to be 78% ID at 24 h post-injection (Fig. 6d).

To evaluate the ability of **FPRR** for imaging of AKI, NIRF and PA imaging were carried out in a mouse model of cisplatin-induced AKI. At 16 h post-treatment of cisplatin, both NIRF and PA signals from the kidneys showed no statistically significant difference from the control group (Fig. 6e). However, at 24 and 48 h post-treatment of cisplatin, the NIRF signals from activated **FPRR** clearly delineated the kidneys, simultaneously PA signals could be observed at the sites of renal parenchyma and pelvis, showing a 1.36-fold (1.97) and 1.54-fold (1.93) increase in NIRF (PA) signals at 24 and 48 h post-treatment of cisplatin, respectively (Fig. 6f). In contrast, both NIRF and PA signals of NAC pretreatment group showed no difference compared to the control group. Although the earliest timepoint for NIRF imaging to detect the upregulation of GGT is the same with PA imaging, PA imaging had a 2.3-fold higher SBR relative to NIRF imaging (Fig. 6g), because PA imaging relies on detection of acoustic signals and has deeper tissue penetration. Thus, **FPRR** represented the first activatable fluoro-PA probe for real-time imaging of AKI.

Activatable probes with low renal clearance efficiencies have also been employed for detection of AKI. However, such probes often failed to real-time detect AKI in living mice because only a limited amount probes can filter into the kidneys. Thus, kidneys are often excised for *ex vivo* imaging. Lin and co-workers have developed a **NIR-O$_2$$^{•-}$** probe based on the positively charged merocyanine dye for detecting AKI by imaging of upregulated O$_2$$^{•-}$ (Fig. 7a).[59] **NIR-O$_2$$^{•-}$** was initially nonfluorescent ($\Phi = 0.01$). Upon addition of O$_2$$^{•-}$, the fluorescence intensity at 719 nm increased with the increase of O$_2$$^{•-}$
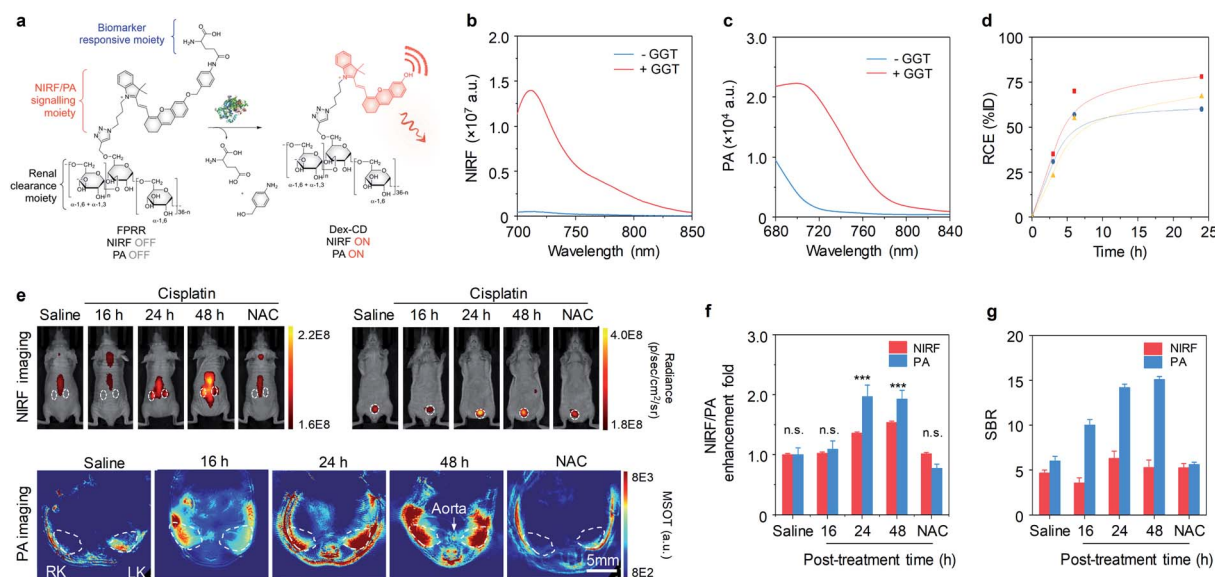

Fig. 6 (a) Chemical structures and molecular mechanism of **FPRR** for NIRF and PA imaging of AKI. (b and c) Fluorescence and PA spectra of **FPRR** (25 μM) in the absence or presence of GGT (20 μg) in PBS buffer (10 mM, pH 7.4). (d) RCE as a function of time post-injection of **FPRR** in living mice. The three lines represent the measurements in three independent mice. (e) Representative NIRF images of living mice at 60 min and PA images (700 nm) of mice transverse section at 120 min after injection of **FPRR** (6.5 μmol per kg body weight) at different time points (0, 16, 24 or 48 h) post-treatment of cisplatin (20 mg per kg body weight). For NAC-protected mice, real-time imaging was conducted at 48 h post-cisplatin treatment. The white circles indicate the site of kidneys and bladder, respectively. NIRF images acquired at 720 nm upon excitation at 675 nm. RK, right kidney; LK, left kidney. (f) Relative NIRF and PA signals enhancement of the kidneys for different treatment groups. (g) Comparison of SBRs between NIRF and PA imaging. n.s.: not significant. *$p < 0.05$, **$p < 0.01$, ***$p < 0.001$. Reproduced with permission from ref. 58. Copyright 2020 John Wiley and Sons.
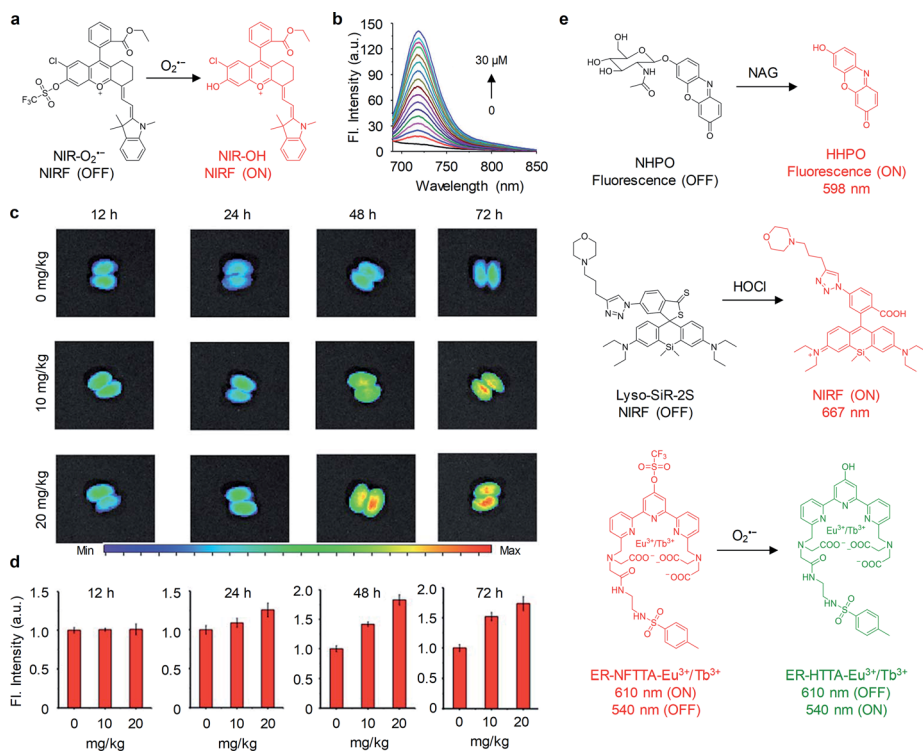
Fig. 7 (a) Chemical structures of $\mathbf{NIR\text{-}O_2}^{\bullet-}$ and its activation form in response to $O_2^{\bullet-}$. (b) Fluorescence spectra of $\mathbf{NIR\text{-}O_2}^{\bullet-}$ (5 μM) in PBS (25 mM, pH 7.4) upon addition of $O_2^{\bullet-}$ (0–30 μM). (c) Representative NIRF images of excised kidneys from mice treated with different doses of cisplatin (0, 10 and 20 mg kg^{-1}) at different post-treatment time points (12, 24, 48 and 72 h). (d) NIRF intensities of the kidneys in panel of c. (e) Chemical structures of probes **NHPO**, **Lyso-SiR-2S** and **ER-NFTTA-Eu3+/Tb3+** and their activation forms in response to NAG, HClO and $O_2^{\bullet-}$, respectively. Reproduced with permission from ref. 59. Copyright 2018 Royal Society of Chemistry.

concentration ($\varPhi = 0.55$), showing a LOD of 0.24 mM (Fig. 7b). To verify the ability of $\mathbf{NIR\text{-}O_2}^{\bullet-}$ to monitor cisplatin-induced AKI, the probe was intravenously injected into mice treated with different doses of cisplatin (0, 10 and 20 mg kg^{-1}). The kidneys from mice at different time points of post-treatment of cisplatin (12, 24, 48 and 72 h) was excised, followed by NIRF imaging. As shown in Fig. 7c and d, increased NIRF signals in the kidneys were observed at 48 h and 72 h post-treatment of cisplatin. In contrast, no significant change in NIRF signals was observed for the control mice and mice treated with cisplatin at 12 h and 24 h post-treatment time points. Thus, $\mathbf{NIR\text{-}O_2}^{\bullet-}$ was able to detect cisplatin-induced AKI.

In parallel with this study, activatable probes including **NHPO**, **Lyso-SiR-2S** and **ER-NFTTA-Eu3+/Tb3+** have been reported for selectively detection of NAG, hypochlorous acid (HClO) and $O_2^{\bullet-}$, respectively, in drug-induced AKI mouse models (Fig. 7e).[60–62] Especially, the probes **Lyso-SiR-2S** and **ER-NFTTA-Eu3+/Tb3+** were functionalized with a morpholine unit and a methylphenyl sulfonamide moiety for lysosome- and endoplasmic reticulum-targeting, respectively, which enabled them to specifically detect ROS in those subcellular locations. Although those activatable probes can monitor respective biomarker in the kidneys, their earliest detection time was delayed as compared with aforementioned MRPs. This was mainly due to their extremely low renal clearance efficiencies, compromising the sensitivity of detection.

3. Ureteral injury

Ureteral injury can cause permanent urinary tract damage, kidney failure, and even mortality if not recognized intra-operatively and timely.[70] Therefore, identification of ureters is essential to preventing ureteral injury and avoid postoperative complications. To date, NIRF probes such as ICG, methylene blue, **ZW800-1**, Genhance750, **UreterGlow** and **2TT-oC6B** dots, *etc.* have been used to intraoperatively visualize ureters.[71,72]

Schnermann and co-workers have reported a water soluble heptamethine cyanine dye **UL-766** for ureter visualization (Fig. 8a).[72] **UL-766** had triethylene glycol chains appended to the two indole groups and a trimethyl-alkyl-ammonium ether group installed on the meso of cyanine polyene, and exhibited the maximum absorption and emission at 766 nm and 789 nm in PBS, respectively. *In vitro* studies demonstrated that **UL-766** had a high stability in serum. However, the commercially available dye **800CW** can react with cellular proteins *via* the *S*-alkylation reaction. To evaluate the ability of **800CW** and **UL-766** for ureter imaging, such two dyes were injected intravenously into rats. As shown in Fig. 8b, **800CW** was mostly accumulated in the bile duct, intestine and kidneys. In contrast, **UL-766** demonstrated exclusive renal clearance with no obvious signal in any organs other than the kidneys or ureters.

Recently, a highly water-soluble NIR dye conjugate of glucosamine (**UreterGlow**) has been reported to visualize ureters
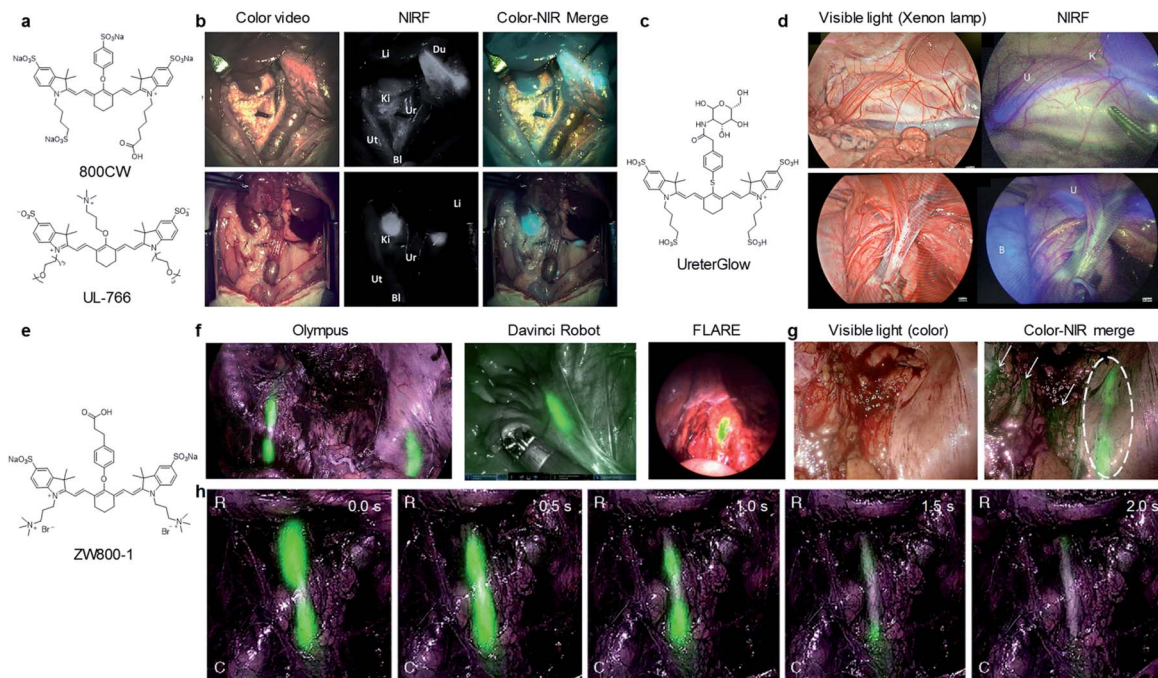
Fig. 8 (a) Chemical structures of **800CW** and **UL-766**. (b) NIRF imaging of ureters after injection of **800CW** and **UL-766**. Liver (Li), duodenum (Du), kidney (Ki), ureter (Ur), uterine (Ut), bladder (Bl). Reproduced with permission from ref. 72. Copyright 2018, Elsevier. (c) Chemical structure of **UreterGlow**. (d) NIRF imaging of ureters at 15 min (upper) and 2 h (bottom) post-injection of **UreterGlow**. Kidney (K), ureter (U), bladder (B). Reproduced with permission from ref. 71. Copyright 2018 American Chemical Society. (e) Chemical structure of **ZW800-1**. (f) NIRF imaging of **ZW800-1** in patients using three different commercial imaging systems. (g) NIRF imaging of ureter under peritoneum. Dashed circle indicated the ureter. Small arrows indicate the vessels in the surrounding tissue. (h) NIRF imaging of ureter flow and patency with **ZW800-1**. The images in panel of g and h were acquired using the Olympus® imaging system. Green signals indicate NIRF of **ZW800-1** and merged with the anatomical images. Reproduced with permission from ref. 70. Copyright 2019 Springer Nature.

in Yorkshire pigs (Fig. 8c and d).[71] **UreterGlow** exhibited an excitation and emission peak at 800 nm and 830 nm in PBS, respectively. It was determined to be highly stable in a pH range from 3.5 to 10, indicating it could be feasible for ureter imaging *in vivo*. Noted that a weakness of some dyes used for ureter imaging was poor emission at an acidic urine. After 15 min intravenous injection of **UreterGlow** into Yorkshire pigs, ureters can be clearly observed with NIRF imaging but invisible under white light illumination. Importantly, the NIRF signal in ureters could be visualized even at 2 h post-injection of **UreterGlow**, suggesting no need of a second injection during abdominal surgeries.

ZW800-1 was a small zwitterionic dye with peak absorption and emission of 770 nm and 788 nm, respectively (Fig. 8e).[70] **ZW800-1** was pharmacologically inert and exhibited renal-exclusive clearance in both small and large animals of preclinical studies. In clinical studies, 5.0 mg of **ZW800-1** dosage did not elicit any acute toxicity and no any hypersensitivity reactions. After administration, **ZW800-1** produced high-quality images for visualization of ureters on all surgical imaging systems such as Olympus®, the Da Vinci® robot, and the FLARE® MIS system (Fig. 8f).

Importantly, the ureters under peritoneum or even under eschar generated by cauterization during cancer resection can be identified (Fig. 8g). Besides, the emitted fluorescence allowed for clear visualization of the motility and patency of the ureter

because of ureteral pulsations (Fig. 8h). Thus, in clinical translation, **ZW800-1** enabled visualization of the anatomical structure as well as flow and patency function of ureters.

Intraureteral injection of non-renal clearable nanoparticles offers another strategy to visualize ureters. Tang and co-workers for the first time reported NIR-II aggregation-induced emission (AIE) dots for intraoperative identification of ureters.[73] As shown in Fig. 9a, water-soluble **2TT-oC6B** dots was prepared *via* precipitation of **2TT-oC6B** with DEPE-PEG. The dots had a spherical morphology with an average diameter of 160 nm and exhibited absorption and emission peak at 733 and 1030 nm, respectively (Fig. 9b and c). Upon continuous laser irradiation for 25 min, **2TT-oC6B** dots exhibited a high photostability with negligible fluorescence decay, while the intensity decreased by over 95% for ICG (Fig. 9d). To evaluate the penetration depth of **2TT-oC6B** dots and ICG, both were injected into the lumen of the ureter anterogradely or retrogradely (Fig. 9e). The NIR-I fluorescence signal of ICG was close to the background noise at a 1.5 cm thickness of beef tissues, whereas the NIR-II fluorescence signal for **2TT-oC6B** dots was still visible even at the chicken tissue thickness of 4.5 cm, indicating **2TT-oC6B** dots had deeper tissue penetration than ICG.

NIR-II fluorescence imaging of intraureteral **2TT-oC6B** dots was carried out in different ureteral models (Fig. 9f). In a ureteral stone model that generated by inserting a foreign body (length/width : 15/1 mm) into the lower ureteral lumen,

Fig. 9 (a) Schematic illustration of the preparation of **2TT-oC6B** dots through nanoprecipitation. (b) Representative TEM image and hydrodynamic diameter of **2TT-oC6B** dots. (c) Absorption and fluorescence spectra of **2TT-oC6B** dots in water. (d) Photostability of **2TT-oC6B** dots and ICG in water. (e) Representative NIR-II images of ureters with retrograde injection of **2TT-oC6B** dots (0.10 mg mL^{-1}) and ICG (0.10 mg mL^{-1}) in the rabbit upon overlaying beef slices with different thicknesses (808 nm, 50 mW cm^{-2}). (f) Representative bright-field and fluorescence images of ureters in different models of foreign body, stricture, abnormal course, complete ligation, or partial ligation. (g) Representative fluorescence images of ureters at different time points of retrogradely post-injection of **2TT-oC6B** dots in rabbit models of complete and partial leakage. (h) Representative fluorescence images of ureters before and after the repair of ureteral injury. Scale bar: 1 cm. Reproduced with permission from ref. 73. Copyright 2020 American Chemical Society.

Fig. 10 (a) Schematic illustration of imaging of APN for detection of bladder cancer using **CyP1** ($R = H$ or $CH_2CHOHCH_3$). (b) Fluorescence spectra of **CyP1** and **CyP2** (30 μM) in the absence or presence of APN (0.5 mg mL^{-1}) in PBS (10 mM, pH 7.4). (c and d) RCE as a function of time post-injection of **CyP1** and **CyP2** in living mice. The three lines represent the measurements in three independent mice. (e) Representative NIRF images of living mice at $t = 0$ and 150 min post-injection of **CyP1** at different time points post tumor implantation. NIRF images acquired at 720 nm upon excitation at 675 nm. (f) NIRF intensities of the bladder in living mice after 150 min injection of **CyP1** at the different time points post tumor implantation. PBS *versus* tumor implantation groups, $*p < 0.05$, $**p < 0.01$, $***p < 0.001$. Reproduced with permission from ref. 75. Copyright 2020 John Wiley and Sons.

Fig. 11 (a) Schematic illustration of the preparation of HSA-MnO$_2$-Ce6 NPs. (b and c) Absorption spectra and hydrodynamic diameters of HSA-MnO$_2$, HSA-Ce6, and HSA-MnO$_2$-Ce6 NPs in PBS. (d) Representative fluorescence images of tumor-bearing mice injected with HSA-Ce6 or HSA-MnO$_2$-Ce6 NPs, and normal mice injected with HSA-MnO$_2$-Ce6 NPs (black dotted circles indicate the bladder area). (e) NIRF intensities of bladder areas at different time points of post-injection of nanoparticles. (f) NIRF intensities of resected major organs in panel d ($n = 3$). Reproduced from ref. 77. Copyright 2018, Creative Commons.

a filling defect from NIR-II fluorescence signal was observed in the ureteral segment (red arrows), implying the presence of the foreign body in the ureteral lumen. In a ureteral stricture model, a filling defect (length: 8 mm, yellow arrow) was clearly observed, suggesting the precise location of the ureteral stricture. Similarly, the abnormal course of the ureter was clearly seen from NIR-II fluorescence signal. In a complete ligation model, the location of the ligation was easily identified from the termination of NIR-II fluorescence signal (yellow arrow). For partial ligation cases, an obvious decline of the fluorescence signal could be observed in the ligation segment of the ureter (red arrows). In a complete leakage model, a large area fluorescence signal was observed after 4 s retrogradely injection of **2TT-oC6B** dot (Fig. 9g, red arrows), indicating NIR-II dots were rapidly leaked to surrounding tissues. In contrast, a small area fluorescence signal was seen for partial leakage cases. Furthermore, **2TT-oC6B** dots were used to evaluate the status of the ureteral repair. As shown in Fig. 9h, retrogradely injected NIR-II dots could delivered across the leakage site without fluorescence signal in surrounding tissues, indicating the successful recanalization of the ureter. Therefore, NIR-II fluorescence imaging of ureters with **2TT-oC6B** dots not only allowed for intraoperative identification of ureters, but also can assess the success of the ureteral repair.

4. Bladder cancer

Bladder cancer is one of the most common malignancies in the urinary system and is associated with high morbidity and mortality.[74] Due to bladder cancer is curable if detected and treated timely, early and accurate diagnostic methods are critical to this disease. As such, several NIRF molecular probes and nanomaterials have been exploited for imaging and intravesical photodynamic diagnosis of bladder cancer.

Recently, our group developed a renal clearable NIRF macromolecular reporter (**CyP1**) for real-time non-invasive imaging of orthotopic bladder cancer in living mice.[75] Because aminopeptidase N (APN) has vital roles in tumour invasion, angiogenesis, and metastasis, and its levels are correlated with tumor size and metastasis stages. Thus, it was chosen as the biomarker for diagnosis of bladder cancer. As shown in Fig. 10a, **CyP1** contained a NIR hemicyanine dye caged by 4-hydroxybenzyl alcohol connected to the alanyl unit, and a HPβCD moiety on the alkyl chain. However, the control probe **CyP2** did not have HPβCD and but had a methyl group on the indole ring. Both **CyP1** and **CyP2** were initially non-fluorescent ($\Phi = 0.007$). In the presence of APN, the amide linkage between the alanyl substrate and the self-immolative linker was cleaved, followed by 1, 6-elimination, eventually leading to the formation of the

'uncaged' fluorophore **CCD** or **CMe** ($\Phi = 0.22$), thus the fluorescence at 720 nm increased by 14-fold and 15-fold for **CyP1** and **CyP2**, respectively (Fig. 10b). After systemic administration of probes into living mice, the renal clearance efficiencies of **CyP1** and **CyP2** were determined to be $94 \pm 2.0\%$ ID and $3.8 \pm 1.6\%$ ID, respectively, at 24 h post-injection (Fig. 10c and d), indicating **CyP1** can be specifically cleared through the kidneys, but **CyP2** failed to do so.

The ability of **CyP1** for real-time imaging of APN was evaluated in a mouse model of orthotopic bladder tumor. **CyP1** was intravenously injected into living mice at different time points after tumor implantation (3, 7, 14, 21, and 28 days). The control mice were implanted with PBS. At 3 days after tumor implantation, the NIRF signal of **CyP1** in the bladder was close to that of the control mice (Fig. 10e). However, the NIRF signals increased by 1.5-, 1.7-, 1.9-, and 2.2-fold relative to the control group at 7, 14, 21, and 28 days post tumor implantation, respectively (Fig. 10f), suggesting the progressively increased level of APN during tumor growth.

Furthermore, **CyP1**-based urinalysis was examined through either direct fluorescence measurement of excreted **CyP1** in the urine from tumor-bearing living mice after its intravenous injection or collection of urine samples from tumor-bearing living mice followed by **CyP1** incubation and fluorescence measurements. The urinalysis results were coincided with *in vivo* NIRF imaging data. In addition, plasma APN produced from other organs cannot be filtered into urine because of its larger molecular weight (*ca.* 110 kDa) relative to the glomerular filtration cutoff (50 kDa).[76] Thereby, **CyP1**-based real-time NIRF imaging and urinalysis could be used for the specific detection of bladder cancer.

Non-renal clearable nanoparticles have also been used for imaging of orthotopic bladder cancer. The accumulated in bladder tumor relied on the enhanced permeability and retention effect. Guo and co-workers reported O^2-generating HSA-MnO$_2$-Ce6 NPs for imaging and enhanced photodynamic therapy of orthotopic bladder cancer in living mice.[77] HSA-MnO$_2$-Ce6 NPs were fabricated with MnO$_2$ NPs, chlorin e6 (Ce6) and human serum albumin (HSA). MnO$_2$ NPs served as the catalyst for convention H$_2$O$_2$ to O$_2$ and the source of Mn^{2+} for magnetic resonance imaging. Ce6 acted as a NIR fluorophore and photosensitizer, while HAS is a reliable drug carrier protein (Fig. 11a). HSA-MnO$_2$-Ce6 NPs had two characteristic absorption peaks at 350 and 670 nm assigned to MnO$_2$ and Ce6, respectively (Fig. 11b). Hydrodynamic diameters of HSA-MnO$_2$, HSA-Ce6, and HSA-MnO$_2$-Ce6 NPs were determined to be 18.5 ± 4.8 nm, 112.8 ± 7.4 nm and 118.6 ± 8.1 nm, respectively (Fig. 11c).

An orthotopic bladder cancer model was established through injection of MB-49 cells into the bladder wall in C57BL/6 mice. *In vivo* NIRF imaging was conducted on tumor-bearing mice after intravenously injection of HSA-Ce6 and HSA-MnO$_2$-Ce6 NPs. At 2 h post-injection of nanoparticles, NIRF signals of Ce6 were observed throughout the mouse body. However, at 12 h post-injection, the liver and bladder of tumor-bearing mice were delineated with NIRF imaging and the signals were further increased at 24 h and 48 h post-injection of nanoparticles

(Fig. 11d). In contrast, the control mice with normal bladder did not show obvious accumulation of HSA-MnO$_2$-Ce6 NPs in the bladder (Fig. 11d). *Ex vivo* imaging of excised major organs at 48 h post-injection further showed that HSA-MnO$_2$-Ce6 NPs was mainly accumulated in liver and tumor-bearing bladder. While barely no fluorescence signal was observed in normal bladder, indicating HSA-MnO$_2$-Ce6 NPs could passively accumulate in bladder tumors for imaging. Moreover, HSA-MnO$_2$-Ce6 NPs was employed to treat orthotopic bladder cancer in mice combined with laser irradiation, showing improved therapeutic efficacy.

Photodynamic diagnosis (PDD) relies on detecting tissue fluorescence from a previously administered photosensitizing agent and drawing diagnostic conclusion through the signal readout.[78] PDD assisted transurethral resection significantly improved the detection of bladder cancer and lowered the recurrence risk relative to the white light transurethral resection.

Pan and co-workers developed a multifunctional nanoporphyrin platform that was coated with a bladder cancer-specific peptide PLZ4.[79] PLZ4-nanoporphyrin-DOX (PNP-DOX) was synthesized through self-assembly of a porphyrin–cholic
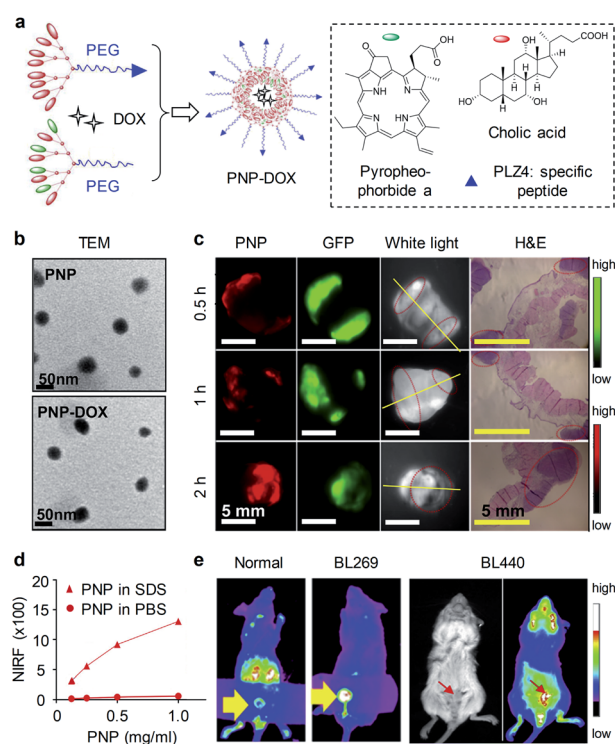

Fig. 12 (a) Schematic illustration of the preparation of PNP and PNP-DOX. The amino acid sequence of PLZ4: cQDGRMGFc. PEG has a molecular weight of 5000 Da. (b) TEM images of PNP and PNP-DOX. (c) PDD images in an MB49-GFP-Luc orthotopic bladder cancer mouse model after 2 h intravesical injection of PNPs (10 mg mL^{-1}). Bladder was harvested and imaged in the GFP (tumor cells) and NIRF channel (PNP uptake) using Kodak imaging station. Yellow lines indicate cut line for histopathology; red circles indicate tumor locations. (d) NIRF intensity of different concentrations of PNPs in PBS and SDS. (e) Representative NIRF images of PNPs in orthotopic PDX BL269 and BL440 bladder cancer mice after intravesical administration of PNPs. Reproduced with permission from ref. 79. Copyright 2016, Elsevier.

acid–PEG conjugate, a cholic acid–PEG conjugate and doxorubicin (DOX), which integrated PDD, image-guided photodynamic therapy, photothermal therapy and targeted chemotherapy in a single procedure (Fig. 12a). PNP and PNP-DOX had spherical morphology with an average diameter of 22 ± 7 and 23 ± 6 nm, respectively (Fig. 12b). PNPs were initially non-fluorescent in PBS. However, PNPs were partially disassociated in the presence of ionic detergent sodium dodecyl sulfate (SDS), resulting in concentration-dependent increase of fluorescence (Fig. 12d). To evaluate the ability of PNPs for PDD of bladder cancer. An orthotopic bladder cancer was established from a green fluorescent protein (GFP) expressing MB49 cell line. The bladders were excised and harvested after intra-urethral injection of PNPs, PNPs fluorescence was observed as early as 30 min within bladder cancer cells and increased in a time-dependent manner (Fig. 12c). However, normal bladder had minimal PNPs uptake. To further validate the clinical application, two different patient-derived xenograft (PDX) models (BL269 and BL440) were established in mice. After intravesical administration of PNPs, bright fluorescence signals were observed in bladders of the orthotopic BL269 and BL440 PDX bladder cancer mice but not in normal bladder (Fig. 12e). In contrast, other major organs gave weak fluorescence signals. Such an efficient and selective uptake ability of PNPs in tumor allowed for PDD of bladder cancer. Moreover, PNP-DOX served as an effective triple-modality therapeutic agent against bladder cancer.

5. Conclusions

Compared with traditional fluorescence imaging in the visible region, NIRF imaging has reduced light attenuation and minimized autofluorescence in biological tissue, allowing for detection of physiological and molecular processes with deeper tissue penetration and improved SBRs. To realize quantitative sensing and imaging *in vivo*, an increasing number of NIRF probes have been developed such as small molecular fluorophores, semiconducting oligomer molecules, inorganic nanoparticles, *etc.* Among them, 'always on' probes with bright fluorescence permitted contrast-enhanced imaging of ureters and kidney dysfunction; while the intrinsic advantages of activatable probes have enabled real-time ultrasensitive detection of pathological biomarkers (*e.g.* ROS and enzymes) for early diagnosis of AKI and bladder cancer.

To extend the applications of NIRF imaging in nephro-urological diseases from its current stage in experimental animal models, and to clinical translatability and applicability, several potential concerns should be addressed.

(i) Kidney: although several NIR fluorophores and ultra-small inorganic nanoparticles can go through renal clearance and are used for kidney imaging, the signal readout from the passive retention in kidneys is unable to diagnose kidney injury at the incipient stage. In contrast, activatable probes can specifically detect AKI-associated biomarkers with an active sensing mechanism, enabling monitor kidney injury early. However, existing activatable probes in NIR-I region still encounters moderate light attenuation and autofluorescence in

tissue. In this regard, NIR-II fluorescence activatable probes are highly demanded. In addition, dual-response probes with two optical channels (such as fluorescence and chemiluminescence) respond to two different biomarkers are highly desirable for improving the accuracy of diseases diagnosis.[57]

(ii) Ureter: ICG and MB are currently the only two NIR fluorophores approved by the Food and Drug Administration (FDA). ICG is not applicable for imaging of ureters because of its hepatic-exclusive clearance. MB is a less favorable fluorophore for ureter visualization due to its suboptimal clearance and fluorescent properties (<700 nm). Intravenous injection of CW800-CA, **UreterGlow** and Genhance750 provided clear delineation of ureters by laparoscopy in a swine model; however, portion of injected fluorophores are eliminated by hepatobiliary clearance, which often contaminates intraoperative images of the abdominal cavity.[80] A series of zwitterionic NIR fluorophores (**ZW800-1**, cRGD-ZW800-1, ZW800-1C) have been discovered for ureteral imaging with valuable features such as low non-specific protein binding and tissue uptake, renal-exclusive clearance and safety. However, their emission wavelengths are in NIR-I window. Although visualization of ureters can be achieved by NIR-II fluorescence imaging of **2TT-oC6B** dots, intraurethral injection of the non-renal clearable dots introduces a risk of ureteral damage during catheter insertion. Thus, an ideal fluorophore for ureter visualization should be safe, renal-exclusive clearable and highly luminescent in NIR-II window. Although aforementioned fluorophores have been tested in a swine model, such studies are insufficient for clinical translation because the ureteral wall of pigs is both thinner and covered by less fat relative to humans.[71]

(iii) Bladder: nanoformulation is generally used to convert intrinsically hydrophobic compounds into water-soluble nanoparticles. Such nanoprecipitation often produces nanoparticles with the size from several ten nanometers to several hundred nanometers,[22] which are larger than the threshold of kidney filtration (~5.5 nm) and are difficult to excrete from kidney to bladder. In addition, the stability of nanoparticles in serum is critical to their use *in vivo*; however, dilution after intravenous injection could lead to nanoparticle disassembly. Although intravenously injected nanoparticles can accumulate into bladder tumors *via* enhanced permeability and retention effect, strong fluorescence in abdomen significantly interferes bladder cancer imaging and gives rise to low SBRs. In contrast, renal-clearable activatable probes can be specifically excreted into bladder and react with tumor-associated biomarkers, providing a new approach for noninvasive imaging and optical urinalysis of bladder cancer. Noted that several bladder tumor biomarkers have been identified for diagnosis, however, none of these biomarkers offer sufficient sensitivity and specificity to be routinely used in the clinics.[81] Thus, to improve the diagnostic accuracy, future generations of activatable probes may rely on the multiplex activations by the correct combination and sequence of multiple biomarkers. In addition, combination of blue light cystoscopy with renal-clearable activatable probes for fluorescence-guided biopsy and resection should be more sensitive than conventional procedures for the detection of malignant tumors, particularly for urothelial carcinoma *in*

situ.[82] Last but not least, PA imaging has increased tissue penetration because it detects acoustic wave that has much less signal attenuation than photons in tissues.[83–86] Thus, development of renal-clearable PA probes is envisioned to improve diagnosis of nephro-urological diseases.

Conflicts of interest

There are no conflicts to declare.

Acknowledgements

Notes and references

1 M. Rudin and R. Weissleder, *Nat. Rev. Drug Discovery*, 2003, **2**, 123–131.
2 J. A. Thomas, *Chem. Soc. Rev.*, 2015, **44**, 4494–4500.
3 Y. Lyu and K. Pu, *Adv. Sci.*, 2017, **4**, 1600481.
4 J. Zhang, P. Cheng and K. Pu, *Bioconjug. Chem.*, 2019, **30**, 2089–2101.
5 Q. Miao and K. Pu, *Adv. Mater.*, 2018, **30**, 1801778.
6 J. Huang and K. Pu, *Angew. Chem., Int. Ed.*, 2020, **59**, DOI: 10.1002/anie.202001783.
7 G. Hong, A. L. Antaris and H. Dai, *Nat. Biomed. Eng.*, 2017, **1**, 1–22.
8 J. Li and K. Pu, *Chem. Soc. Rev.*, 2019, **48**, 38–71.
9 J. Chan, S. C. Dodani and C. J. Chang, *Nat. Chem.*, 2012, **4**, 973–984.
10 B. Li, L. Lu, M. Zhao, Z. Lei and F. Zhang, *Angew. Chem., Int. Ed.*, 2018, **57**, 7483–7487.
11 Y. Hong, J. W. Lam and B. Z. Tang, *Chem. Soc. Rev.*, 2011, **40**, 5361–5388.
12 P. Gao, W. Pan, N. Li and B. Tang, *Chem. Sci.*, 2019, **10**, 6035–6071.
13 X. Zheng, W. Zhu, F. Ni, H. Ai, S. Gong, X. Zhou, J. L. Sessler and C. Yang, *Chem. Sci.*, 2019, **10**, 2342–2348.
14 D. T. Quang and J. S. Kim, *Chem. Rev.*, 2010, **110**, 6280–6301.
15 O. S. Oliinyk, A. A. Shemetov, S. Pletnev, D. M. Shcherbakova and V. V. Verkhusha, *Nat. Comm.*, 2019, **10**, 1–13.
16 Y. Yang, Q. Zhao, W. Feng and F. Li, *Chem. Rev.*, 2013, **113**, 192–270.
17 A. Heuer-Jungemann, N. Feliu, I. Bakaimi, M. Hamaly, A. Alkilany, I. Chakraborty, A. Masood, M. F. Casula, A. Kostopoulou and E. Oh, *Chem. Rev.*, 2019, **119**, 4819–4880.
18 C. Li, W. Li, H. Liu, Y. Zhang, G. Chen, Z. Li and Q. Wang, *Angew. Chem., Int. Ed.*, 2020, **59**, 247–252.
19 J. Li, J. Huang, Y. Lyu, J. Huang, Y. Jiang, C. Xie and K. Pu, *J. Am. Chem. Soc.*, 2019, **141**, 4073–4079.
20 Q. Miao, C. Xie, X. Zhen, Y. Lyu, H. Duan, X. Liu, J. V. Jokerst and K. Pu, *Nat. Biotechnol.*, 2017, **35**, 1102–1110.
21 A. J. Shuhendler, K. Pu, L. Cui, J. P. Uetrecht and J. Rao, *Nat. Biotechnol.*, 2014, **32**, 373–380.
22 Y. Jiang and K. Pu, *Acc. Chem. Res.*, 2018, **51**, 1840–1849.
23 X. Zhen and K. Pu, *Nano Res.*, 2018, **11**, 5258–5280.
24 X. Zhen, C. Zhang, C. Xie, Q. Miao, K. L. Lim and K. Pu, *ACS Nano*, 2016, **10**, 6400–6409.
25 H. Gong, R. Peng and Z. Liu, *Adv. Drug Deliv. Rev.*, 2013, **65**, 1951–1963.
26 A. Fernández and M. Vendrell, *Chem. Soc. Rev.*, 2016, **45**, 1182–1196.
27 L. Wu, A. C. Sedgwick, X. Sun, S. D. Bull, X. P. He and T. D. James, *Acc. Chem. Res.*, 2019, **52**, 2582–2597.
28 W. Feng, Y. Zhang, Z. Li, S. Zhai, W. Lv and Z. Liu, *Anal. Chem.*, 2019, **91**, 15757–15762.
29 Y. Fang, W. Shi, Y. Hu, X. Li and H. Ma, *Chem. Comm.*, 2018, **54**, 5454–5457.
30 A. Liapis, P. Bakas, V. Giannopoulos and G. Creatsas, *Int. Urogynecol. J.*, 2001, **12**, 391–394.
31 J. A. Gross, B. E. Lehnert, K. F. Linnau, B. B. Voelzke and C. K. Sandstrom, *Radiol. Clin.*, 2015, **53**, 773–788.
32 J. Klein, J. L. Bascands, H. Mischak and J. P. Schanstra, *Kidney Int.*, 2016, **89**, 539–545.
33 C. D. Scales, G. E. Tasian, A. L. Schwaderer, D. S. Goldfarb, R. A. Star and Z. Kirkali, *Clin. J. Am. Soc. Nephrol.*, 2016, **11**, 1305–1312.
34 K. Kuno, A. Menzin, H. H. Kauder, C. Sison and D. Gal, *Urology*, 1998, **52**, 1004–1008.
35 F. Matsui, F. Matsumoto and K. Shimada, *J. Pediatr. Surg.*, 2007, **42**, e7–10.
36 B. Jordan and J. J. Meeks, *Nat. Rev. Urol.*, 2019, **16**, 23–34.
37 V. Dandolu, E. Mathai, A. Chatwani, O. Harmanli, M. Pontari and E. Hernandez, *Int. Urogynecol. J. Pelvic. Floor Dysfunct.*, 2003, **14**, 427–431.
38 D. Ye, A. J. Shuhendler, L. Cui, L. Tong, S. S. Tee, G. Tikhomirov, D. W. Felsher and J. Rao, *Nat. Chem.*, 2014, **6**, 519–526.
39 F. Xu, H. Li, Q. Yao, H. Ge, J. Fan, W. Sun, J. Wang and X. Peng, *Chem. Sci.*, 2019, **10**, 10586–10594.
40 R. Tian, W. Sun, M. Li, S. Long, M. Li, J. Fan, L. Guo and X. Peng, *Chem. Sci.*, 2019, **10**, 10106–10112.
41 A. S. Jeevarathinam, J. E. Lemaster, F. Chen, E. Zhao and J. V. Jokerst, *Angew. Chem., Int. Ed.*, 2020, **59**, 4678–4683.
42 X. Zhen, J. Zhang, J. Huang, C. Xie, Q. Miao and K. Pu, *Angew. Chem., Int. Ed.*, 2018, **57**, 7804–7808.
43 K. Shou, Y. Tang, H. Chen, S. Chen, L. Zhang, A. Zhang, Q. Fan, A. Yu and Z. Cheng, *Chem. Sci.*, 2018, **9**, 3105–3110.
44 F. Wu, S. G. Bhansali, W. C. Law, E. J. Bergey, P. N. Prasad and M. E. Morris, *Pharm. Res.*, 2012, **29**, 1843–1853.
45 X. Qian and Z. Xu, *Chem. Soc. Rev.*, 2015, **44**, 4487–4493.
46 B. Kim, M. Fukuda, J. Y. Lee, D. Su, S. Sanu, A. Silvin, A. T. T. Khoo, T. Kwon, X. Liu, W. Chi, X. Liu, S. Choi, D. S. Y. Wan, S. J. Park, J. S. Kim, F. Ginhoux, H. S. Je and Y. T. Chang, *Angew. Chem., Int. Ed.*, 2019, **58**, 7972–7976.
47 E. E. Nesterov, J. Skoch, B. T. Hyman, W. E. Klunk, B. J. Bacskai and T. M. Swager, *Angew. Chem., Int. Ed.*, 2005, **44**, 5452–5456.

48 P. Gao, W. Pan, N. Li and B. Tang, *Chem. Sci.*, 2019, **10**, 6035–6071.

49 H. Li, Y. Li, Q. Yao, J. Fan, W. Sun, S. Long, K. Shao, J. Du, J. Wang and X. Peng, *Chem. Sci.*, 2019, **10**, 1619–1625.

50 P. Cheng, Q. Miao, J. Li, J. Huang, C. Xie and K. Pu, *J. Am. Chem. Soc.*, 2019, **141**, 10581–10584.

51 J. Huang and N. Gretz, *ChemistryOpen*, 2017, **6**, 456–471.

52 H. S. Choi, W. Liu, P. Misra, E. Tanaka, J. P. Zimmer, B. Itty Ipe, M. G. Bawendi and J. V. Frangioni, *Nat. Biotechnol.*, 2007, **25**, 1165–1170.

53 A. A. Burns, J. Vider, H. Ow, E. Herz, O. Penate-Medina, M. Baumgart, S. M. Larson, U. Wiesner and M. Bradbury, *Nano Lett.*, 2009, **9**, 442–448.

54 H. Kang, J. Gravier, K. Bao, H. Wada, J. H. Lee, Y. Baek, G. El Fakhri, S. Gioux, B. P. Rubin, J. L. Coll and H. S. Choi, *Adv. Mater.*, 2016, **28**, 8162–8168.

55 B. Du, X. Jiang, A. Das, Q. Zhou, M. Yu, R. Jin and J. Zheng, *Nat. Nanotechnol.*, 2017, **12**, 1096–1102.

56 J. Huang, J. Li, Y. Lyu, Q. Miao and K. Pu, *Nat. Mater.*, 2019, **18**, 1133–1143.

57 J. Huang, Y. Lyu, J. Li, P. Cheng, Y. Jiang and K. Pu, *Angew. Chem., Int. Ed.*, 2019, **58**, 17796–17804.

58 P. Cheng, W. Chen, S. Li, S. He, Q. Miao and K. Pu, *Adv. Mater.*, 2020, **32**, e1908530.

59 Y. Lv, C. Dan, S. Dongdong, M. Chen, B. C. Yin, L. Yuan and X. B. Zhang, *Chem. Sci.*, 2018, **9**, 7606–7613.

60 F. Yan, X. Tian, Z. Luan, L. Feng, X. Ma and T. D. James, *Chem. Commun.*, 2019, **55**, 1955–1958.

61 J. Wang, D. Cheng, L. Zhu, P. Wang, H. W. Liu, M. Chen, L. Yuan and X. B. Zhang, *Chem. Commun.*, 2019, **55**, 10916–10919.

62 Z. Tang, B. Song, W. Zhang, L. Guo and J. Yuan, *Anal. Chem.*, 2019, **91**, 14019–14028.

63 B. Du, X. Jiang, Y. Huang, S. Li, J. C. Lin, M. Yu and J. Zheng, *Bioconjug. Chem.*, 2020, **31**, 241–247.

64 M. Yu, J. Zhou, B. Du, X. Ning, C. Authement, L. Gandee, P. Kapur, J. T. Hsieh and J. Zheng, *Angew. Chem., Int. Ed.*, 2016, **55**, 2787–2791.

65 M. N. Tantawy, R. Jiang, F. Wang, K. Takahashi, T. E. Peterson, D. Zemel, C. M. Hao, H. Fujita, R. C. Harris, C. C. Quarles and T. Takahashi, *BMC Nephrol*, 2012, **13**, 168.

66 J. Huang, C. Xie, X. Zhang, Y. Jiang, J. Li, Q. Fan and K. Pu, *Angew. Chem., Int. Ed.*, 2019, **58**, 15120–15127.

67 J. Huang, S. Weinfurter, P. C. Pinto, M. Pretze, B. Kranzlin, J. Pill, R. Federica, R. Perciaccante, L. D. Ciana, R. Masereeuw and N. Gretz, *Bioconjug. Chem.*, 2016, **27**, 2513–2526.

68 J. Huang, S. Weinfurter, C. Daniele, R. Perciaccante, R. Federica, L. Della Ciana, J. Pill and N. Gretz, *Chem. Sci.*, 2017, **8**, 2652–2660.

69 J. Huang, N. Gretz and S. Weinfurter, *Eur. J. Pharmacol.*, 2016, **790**, 92–98.

70 K. S. de Valk, H. J. Handgraaf, M. M. Deken, B. G. Sibinga Mulder, A. R. Valentijn, A. G. Terwisscha van Scheltinga, J. Kuil, M. J. van Esdonk, J. Vuijk, R. F. Bevers, K. C. Peeters, F. A. Holman, J. V. Frangioni, J. Burggraaf and A. L. Vahrmeijer, *Nat. Commun.*, 2019, **10**, 3118.

71 S. M. Mahalingam, F. Dip, M. Castillo, M. Roy, S. D. Wexner, R. J. Rosenthal and P. S. Low, *Mol. Pharm.*, 2018, **15**, 3442–3447.

72 J. Cha, R. R. Nani, M. P. Luciano, G. Kline, A. Broch, K. Kim, J. Namgoong, R. A. Kulkarni, J. L. Meier, P. Kim and M. J. Schnermann, *Bioorg. Med. Chem. Lett.*, 2018, **28**, 2741–2745.

73 J. Du, S. Liu, P. Zhang, H. Liu, Y. Li, W. He, C. Li, J. H. C. Chau, R. T. K. Kwok, J. W. Y. Lam, L. Cai, Y. Huang, W. Zhang, J. Hou and B. Z. Tang, *ACS Appl. Mater. Inter.*, 2020, **12**, 8040–8049.

74 S. A. Funt and J. E. Rosenberg, *Nat. Rev. Clin. Oncol.*, 2017, **14**, 221–234.

75 J. Huang, Y. Jiang, J. Li, S. He, J. Huang and K. Pu, *Angew. Chem., Int. Ed.*, 2020, **59**, 4415–4420.

76 A. Ruggiero, C. H. Villa, E. Bander, D. A. Rey, M. Bergkvist, C. A. Batt, K. Manova-Todorova, W. M. Deen, D. A. Scheinberg and M. R. McDevitt, *Proc. Natl. Acad. Sci. U. S. A.*, 2010, **107**, 12369–12374.

77 T. Lin, X. Zhao, S. Zhao, H. Yu, W. Cao, W. Chen, H. Wei and H. Guo, *Theranostics*, 2018, **8**, 990–1004.

78 J. A. Witjes and J. Douglass, *Nat. Clin. Pract. Urol.*, 2007, **4**, 542–549.

79 T. Y. Lin, Y. Li, Q. Liu, J. L. Chen, H. Zhang, D. Lac, H. Zhang, K. W. Ferrara, S. Wachsmann-Hogiu, T. Li, S. Airhart, R. deVere White, K. S. Lam and C. X. Pan, *Biomaterials*, 2016, **104**, 339–351.

80 M. D. Slooter, A. Janssen, W. A. Bemelman, P. J. Tanis and R. Hompes, *Tech. Coloproctol.*, 2019, **23**, 305–313.

81 A. C. Woodman, S. Goodison, M. Drake, J. Noble and D. Tarin, *Clin. Cancer Res.*, 2000, **6**, 2381–2392.

82 W. S. Tan and J. D. Kelly, *Nat. Rev. Urol.*, 2018, **15**, 667–685.

83 Y. Jiang and K. Pu, *Adv. Biosys.*, 2018, **2**, 1700262.

84 Y. Jiang and K. Pu, *Small*, 2017, **13**, 1700710.

85 Y. Lyu, J. Li and K. Pu, *Small Methods*, 2019, **3**, 1900553.

86 D. Cui, P. Li, X. Zhen, J. Li, Y. Jiang, A. Yu, X. Hu and K. Pu, *Adv. Funct. Mater.*, 2019, **29**, 1903461.